GT2025-153540

EXAMINING THE POTENTIAL OF HIGH-ORDER SRS TO SUPPORT RANS-BASED COMPRESSOR AIRFOIL OPTIMIZATION

Georgios Goinis*, Sutharsan Satcunanathan, Michael Bergmann

German Aerospace Center (DLR), Institute of Propulsion Technology, Linder Höhe, 51147 Cologne, Germany

ABSTRACT

Turbomachinery aerodynamic optimizations are predominantly carried out using RANS-based CFD. The approach has reached a high level of maturity over the past years through extensive practical experience. With the ever-increasing demands on designs, the demands on simulation accuracy are also increasing, and efforts are being made to incorporate scale-resolved simulations (SRS) into the design process of turbomachinery. Although SRS still remain too costly for primary use in industrial optimization, ongoing advancements favor its gradual integration. This is supported by design trends such as smaller core engines, resulting in locally reduced Reynolds numbers. Potential boundary layer separation and a high level of unsteadiness in these low Reynolds number flows amplify the uncertainties of RANS. At the same time the computational requirements of SRS are drastically reduced due to the reduced bandwidth of turbulent scales. To assess the potential of utilizing SRS in optimization frameworks, RANS-optimized airfoils are re-evaluated with Large-Eddy Simulations (LES) based on a high-order Discontinuous Galerkin solver. First, a RANS optimization is performed for a low Reynolds number airfoil with the aim of reducing the loss at the design point and increasing the operating range, while adhering to a constraint of nearly axial outflow angle. A subset of Pareto-front geometries is then re-simulated using LES to assess the impact of the chosen CFD methodology on the optimization result. Detailed flow analyses give insights on the deficiencies of RANS. The results demonstrate how optimizations can be driven into a suboptimal direction when relying solely on RANS, underscoring the necessity of incorporating SRS into the process and providing initial insights into how this can be done. It is demonstrated how data obtained from only a few SRS can be fed back into the optimization process, leading to an improved optimization outcome.

Keywords: Optimization, Compressor, Cascade, OGV, RANS, LES

NOMENCLATURE

Abbreviations	

ADP aerodynamic design point AVDR axial-velocity-density-ratio CFD computational fluid dynamics

LE leading edge

LES large-eddy simulation MP measurement plane OP operating point

RANS Reynolds-averaged Navier-Stokes SRS scale resolving simulations STG synthetic turbulence generator

TE trailing edge

Roman letters

c chord

 c_f skin friction coefficient d distance to the wall p static pressure

 p_t stagnation (total) pressure

t pitch, thickness x, y, z Cartesian coordinates L_T turbulence length scale

Ma Mach number
Re Reynolds number
T static temperature
Tu Turbulence intensity

V volume

Greek letters

 α flow angle, measured from x-axis in

counterclockwise direction at inlet and clockwise

direction at MP2

 β metal angle, measured from chord

 $d\beta$ wedge angle on suction side

 γ stagger angle, measured from x-axis

 σ viscous stress tensor

au shear stress

Δ cell size

^{*}Corresponding author: georgios.goinis@dlr.de

Superscripts and subscripts

□ averaging in the homogeneous dimensions time and spanwise direction
□ Favre-averaged quantity (temporally) $\langle \Box \rangle_a \qquad \text{area-weighted averaging} := \frac{1}{\int da} \int \Box da$ $\{\Box \}_a \qquad \text{mass flow-weighted averaging} := \frac{1}{\int \rho u \Box da} \int \rho u \Box da$

i,j,kcartesian vector componentsx,y,zCartesian vector components

w value on the wall
rel relative values
1,2 values at MP1/MP2
in,out values at CFD inlet/outlet

1. INTRODUCTION

The aerodynamic design and optimization processes of turbomachinery heavily rely on Reynolds-Averaged Navier-Stokes (RANS) simulations. Design approaches based on RANS, embedded in well-developed computational workflows, offer reliable solutions for standard design conditions but face significant limitations when applied to more complex, unsteady flow scenarios. While RANS remains a key design tool, the inherent modelling that accounts for turbulent effects is prone to inaccuracies and uncertainties. Therefore RANS-CFD becomes increasingly inaccurate in conditions that differ from steady flows. That is particularly the case for designs involving complex secondary flows and flow separation near operating limits. These limitations undermine the reliability of RANS-CFD as a general design tool, resulting in large safety margins and limited design freedom, preventing the exploration of radically new designs and sometimes imposing the choice of sub-optimal operating conditions.

With increasing demands for ultra-efficient, low-emission propulsion systems and components, such as unducted low-noise fans and compact core engines, the industry faces new challenges that exceed the capabilities of conventional RANS-based methods. Scale-Resolving Simulations (SRS), including Large Eddy Simulation (LES), have the potential to provide better predictions, offering significantly reduced modeling uncertainty and enhanced accuracy, specifically when applied to design problems where RANS methods struggle to produce accurate solutions. The downside of SRS is the computational cost. SRS are often 100 to 1000 times more resource-intensive than RANS. Advancements in high-order numerical methods, GPU-based computing, and machine learning now offer pathways for integrating SRS into industrial design processes. However, SRS still remains impractical as the main simulation tool of routine design optimizations.

Fig. 1 exemplarily shows the results of an optimization performed with MISES [1, 2], an inviscid blade-to-blade solver coupled to the integral boundary layer equations to account for viscous effects, of the compressor airfoil used for the studies in this paper. In addition, RANS re-simulations of the MISES Pareto-front and a full RANS-based optimization are plotted. The MISES Pareto-front evaluated with RANS shows that these geometries are performing much worse than the RANS-optimized Pareto-front geometries. This highlights how optimization procedures based on lower-fidelity design tools will converge to suboptimal solutions, as the optimizer exploits any uncertainty of the

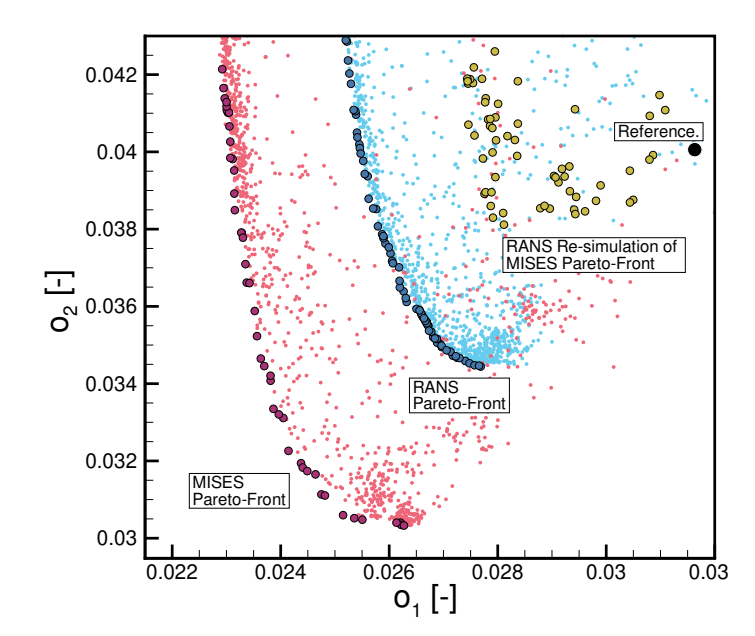


FIGURE 1: Example of a sub-optimal optimization result due to a lower fidelity flow solver MISES compared to a higher fidelity RANS solver. Plotted are data bases of a compressor airfoil optimization with the aim of minimizing o_1 and o_2 . Data base (•) and Pareto-front (•) obtained using MISES as a flow solver, data base (•) and Pareto-front (•) using a RANS flow solver, and re-simulation of MISES-optimized Pareto-front using RANS (•).

underlying models. This problem has been shown with different design tools on different levels of the aero engine design process (e.g. [3, 4]). The fundamental difficulty arises when the high-fidelity model is not a viable option for use in the optimization process as the main evaluation tool due to its prohibitively high cost, as is the case with SRS.

Therefore, if an accuracy of SRS is needed, it is of high interest to include as much information gathered from few SRS into standard RANS optimization procedures. A feasible and robust methodology to combine SRS and RANS is yet to be found, but especially the use of multi-fidelity surrogates, such as Co-Kriging [5, 6] combining RANS and SRS appears to be attractive. However, it would require a good correlation between the high-and low-fidelity models to be effective. This is not guaranteed, especially in regions of the design space where RANS models deviate considerably from the SRS reference. Furthermore the surrogates would have to deal with extremely sparse high-fidelity (SRS) data. Another promising methodology in this context is the use of LES-augmented RANS approaches, such as data-driven turbulence modeling.

In this paper we examine the potential of SRS to support RANS-based optimizations. This can be regarded as a first step in developing an optimization methodology with the ultimate aim of providing the accuracy of SRS in an optimization but at the cost of only a limited number of SRS simulations. A low-Reynolds-number compressor cascade is used as a test vehicle, representative of current challenges in compressor designs dealing with locally reduced Reynolds numbers and, hence, large flow separations, and at the same time simple enough to test and

TABLE 1: Cascade design parameters

Inflow Mach number Ma ₁	0.60
Inflow Reynolds number Re ₁	1.5×10^{5}
Inflow angle α_1	43°
Turbulence intensity Tu	0.5 %
Chord length c	70mm
Pitch to chord ratio b/c	0.577
Height to chord ratio h/c	2.4
Stagger angle γ	16.04°
AVDR	1.03

validate different strategies. First, a RANS-only optimization is performed to identify the Pareto-optimal members. A subset of these are re-assessed using high-fidelity SRS. The differences to the RANS results and the projected consequences for the optimization outcome are discussed in detail.

Based on the observed differences between SRS and RANS, the settings of the RANS optimization are adjusted in a second optimization step to enhance the overall outcome. This manual intervention is feasible due to the simplicity of the 2D geometry but is unlikely to scale efficiently to industry-relevant 3D cases. Nevertheless, this study serves as a demonstration of how high-fidelity models can be leveraged to augment RANS within an optimization framework and represents an initial step toward a fully automated SRS-assisted optimization approach.

2. OPTIMIZATION SETUP

The reference geometry for the study is a compressor airfoil, which has originally been developed as an outlet guide vane of a low pressure turbine stage in a small turbofan engine [7, 8] and has then been further optimized for the application of riblets [9]. An overview of the general design parameters is given in Tab. 1. Extensive experiments were carried out on the reference airfoil in the Transonic Cascade Wind Tunnel [10, 11] at the DLR in Cologne, complemented by recently conducted RANS and LES [12].

2.1 Optimizer

The optimization was carried out using DLR's optimization tool *AutoOpti*. *AutoOpti* is a multi-objective optimization framework based on evolutionary algorithms supported by surrogate models. It has been successfully applied in numerous studies related to the design of compressors [3, 13–15].

The overall aim of the optimization is to reduce the airfoil losses, especially at design point, while maintaining a certain operating range and axial outflow conditions. Kriging surrogate models are employed to accelerate the optimization convergence.

Parameterization The profile is parameterized using 21 engineering design parameters using *BladeGen* [16] as illustrated in Fig. 2. Additionally, the pitch t is allowed to vary, which amounts to a total of 22 free design variables. The admissible ranges for pitch and the different angles are provided in Tab. 2. The suction side of the airfoil is parameterized using a spline with six control points ($CP_{i,x}|CP_{i,y}$). The first and last points are fixed, leaving four control points adjustable in two dimensions,

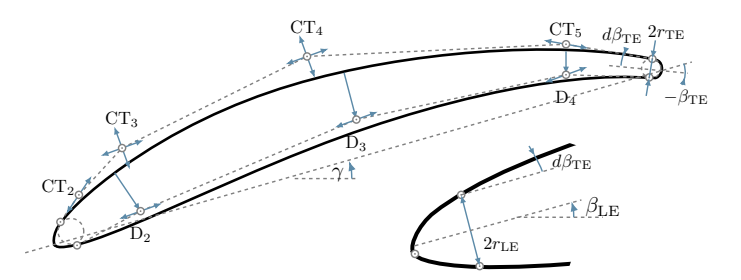


FIGURE 2: Illustration of the profile parameterization. Parameters refining the LE shape are not shown.

TABLE 2: Range of selected optimization parameters

Parameter		min.	reference	max.
	4 F1			
pitch	<i>t</i> [m]	0.028	0.040	0.053
stagger angle	γ [°]	14.0	16.0	19.0
LE angles	$eta_{ m LE}$ [°]	22.0	31.7	36.0
	$d\beta_{\rm LE}$ [°]	0.0	18.3	32.0
TE analas	$eta_{ ext{TE}}$ [°]	-30.0	-26.0	-22.0
TE angles	$d\beta_{\mathrm{TE}}$ [°]	0.0	3.2	10.0
LE radius	$r_{ m LE}/c$	0.005	0.0076	0.01
TE radius	r_{TE}/c	0.005	0.0077	0.015

yielding a total of eight free parameters. Similarly, a spline with five control points is used for a thickness distribution indirectly defining the pressure side. The middle three control points are free to be shifted $(D_{i,x}|D_{i,y})$, i.e. yielding six free parameters. Additionally, two parameters are dedicated to shaping the leading edge, including the possibility of asymmetry between the upper and lower surface.

Operating points Three operating points at $Ma_{in} = 0.6$ and $Re_{in} = 1.5 \times 10^5$ were simulated for each geometry. One at the aerodynamic design point (ADP) OPADP and two at off-design operating points differing from the ADP by a ±5° incidence, which are termed OP+ and OP- hereafter. The off-design operating points are used to judge the operating range in terms of off-design losses and outflow angles. The difficulty arises from the fact, that both the flow velocities and the thermodynamic state at the inlet are prescribed, exceeding the number of allowed inflow boundary conditions for a well-defined problem of a subsonic flow. The solution to this problem in the RANS and LES is described further below. Note, that in a previous study [12] the simulations were set up to match the available experimental conditions, in particular the back-pressure. Therefore the results of the reference geometry, which have been taken from the previous study [12], should be compared to the other results of this study with caution.

Objectives Two objective functions were defined, aiming at reducing the losses at design point and off-design:

$$o_1 := \min(\omega_{\text{ADP}})! \tag{1}$$

$$o_2 := \min\left(\frac{\omega_{\text{OP}^-} + \omega_{\text{OP}^+}}{2}\right)! \tag{2}$$

TABLE 3: Initial optimization constraints

Quantity	min	max.
$\alpha_{2.\mathrm{ADP}}$	-0.2	1.4
$\alpha_{2.\mathrm{OP+}}$	-1.4	2.6
$\alpha_{2.\mathrm{OP-}}$	-1.4	2.6
$t_{ m max}$	0.05	0.09
$c_{t,max}$	0.34	0.51
profile area	0.041	0.062
center of gravity x	0.37	0.56

where

$$\omega = \frac{\left\{\overline{p_{t,1}}\right\}_{y} - \left\{\overline{p_{t,2}}\right\}_{y}}{\left\{\overline{p_{t,1}}\right\}_{y} - \left\langle\overline{p_{1}}\right\rangle_{y}}.$$
(3)

By default the operation $\overline{\square}$ was used. Results using an alternative Favre-averaging $\widetilde{\square}$ will also be shown for better comparability with solutions obtained with the compressible RANS equations. The averaging $\overline{\square}$ is redundant in RANS.

Constraints Geometric and aerodynamic constraints were applied (Tab. 3). To avoid local minima in the thickness distribution the spline parameters were constrained accordingly and the geometries checked during the optimization. To enforce axial outflow, α_2 was constrained at all operating points, with relaxed limits at the two off-design points.

2.2 Numerical Setup

The numerical flow simulations, i.e. RANS and LES, have been performed with DLR's solver for turbomachinery flows *TRACE*.

2.2.1 RANS. The RANS simulations are performed using a density-based Finite-Volume discretization on block-structured meshes. A MUSCL scheme with Van-Albada 1 limiter in combination with Roe's approximate Riemann solver is used to discretize the convective fluxes and central derivatives are employed for the viscous fluxes to obtain second-order accuracy in space. In order to derive the steady state solutions, the five conservation equations are solved in a coupled manner using an implicit dual time-stepping approach. The additional turbulence model equations are solved implicitly in a conservative but segregated manner [17]. In the present study, we employ Menter's SST $k-\omega$ model in the 2003 version [18] with stagnation point fix of Kato and Launder [19]. The transition from laminar to turbulent flow is modelled by the two-equation γ -Re_{θ} model [20]. At the inflow and outflow boundaries, two-dimensional non-reflecting boundary conditions are used [21]. At all OPs a controller was used to reach the target Main by adjusting the back-pressure. Periodic boundary conditions are used in the pitchwise, and inviscid walls in the spanwise direction. The effect of the AVDR is modelled via a source term

$$S = \frac{1}{h} \frac{\partial h}{\partial x} \left([0, p, 0, 0, 0]^T - F_{\text{adv}}^x \right)$$
 (4)

following Giles [22] and Bolinches et al. [23], where p is the static pressure, h the height of the channel, x the axial coordinate

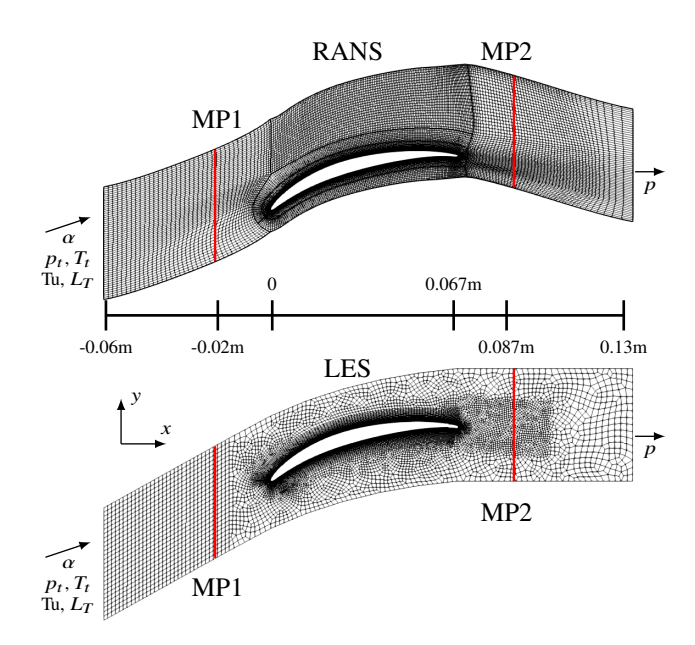


FIGURE 3: RANS and LES domain and mesh in the *x-y* plane for the reference geometry. For the LES, only the high-order grid cells are shown and the solution nodes, i.e. 25 in each 2D element, are omitted for better visibility.

and F_{adv}^x the advective flux vector in the axial direction. The contraction of the channel height is modelled from the blade's leading edge towards the trailing edge and shaped with a sinusoidal distribution, i.e.

$$h(x) = \frac{h_{LE} - h_{TE}}{2} \left[\cos \left(\frac{x - x_{LE}}{x_{TE} - x_{LE}} \pi \right) + 1 \right] + h_{TE}.$$
 (5)

The same mesh resolution has been used for all RANS simulations, created with the in-house meshing tool PyMesh using an O-C-H topology [24]. The grid-converged mesh consists of 28 000 hexahedral elements. The domain and mesh are shown in Fig. 3. Probes are used to extract the mean flow values at several positions, i.e. MP1, MP2 or boundary layer cuts, ensuring consistency with the LES.

2.2.2 LES. The LES simulations have been performed with the high-order discontinuous Galerkin (DG) solver of TRACE, which has been thoroughly validated on, and successfully applied to various turbomachinery-related configurations, cf. [25– 29]. The implicitly filtered Navier-Stokes equations are first transformed into the reference system with a high-order polynomial mapping, which ensures free-stream preservation. The solution and fluxes are approximated via one-dimensional 4thorder Legendre polynomials with Legendre-Gauss-Lobatto basis nodes, which are extended to 3D in a tensor-product fashion. The numerical integration is performed with Legendre-Gauss-Lobatto quadrature, collocated with the solution approximation. The viscous terms are discretized using the Bassi and Rebay 1 scheme [30]. Adjacent elements are coupled via Roe's approximate Riemann solver for the advective part and central fluxes for the viscous part. Stabilization for under-resolved turbulent flows is achieved by using a split formulation of the discontinuous Galerkin spectral element method (DGSEM) following Gassner

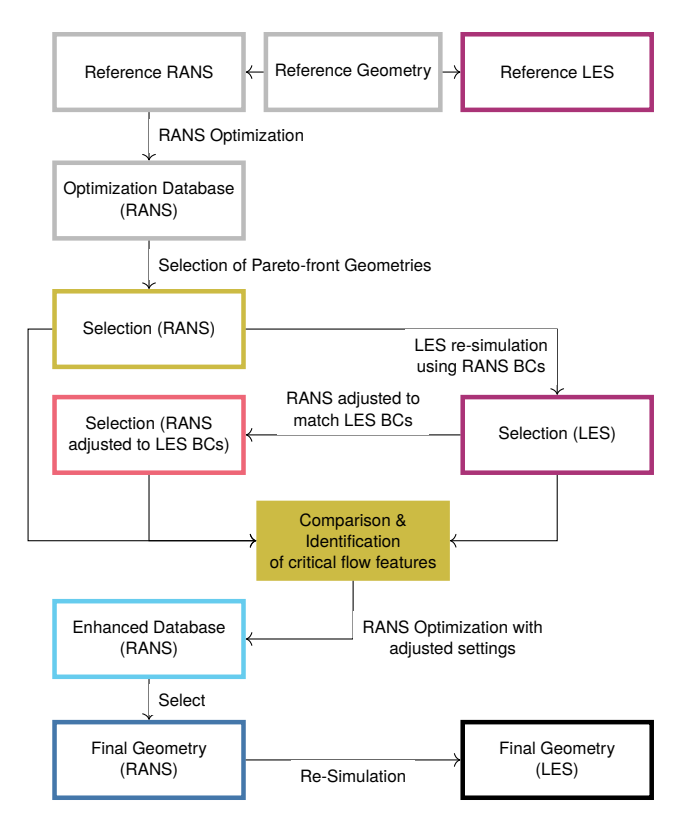


FIGURE 4: Study outline. Colours correspond to those in Fig. 5.

et al. [31]. In this present study, Kennedy-Gruber's kineticenergy preserving two-point fluxes are used [32]. The resulting discretization achieves a 5th-order accuracy on unstructured hexahedral grids. The time-integration is performed by employing a strong-stability preserving third-order explicit Runge-Kutta scheme of Shu and Osher [33].

Riemann and one-dimensional non-reflecting boundary conditions are used at the inflow and outflow, respectively, cf. [21]. Inflow turbulence is generated synthetically at the inflow plane by a synthetic turbulence generator (STG), originally proposed by Shur et al. [34], and implemented and validated in [35, 36]. The STG is based on a superposition of Fourier modes with random phases and direction vectors, which produce a modified von Karman spectrum. The fluctuations of the STG are added onto the boundary state derived from the boundary conditions and are weakly imposed over the flux. Periodicity is enforced in the pitchand spanwise direction. Similar to RANS, the source term Eq. (4) is used to model the effect of the AVDR on the mid-section. The current non-reflecting in- and outflow boundary conditions, as typically used in turbomachinery applications, require the total pressure $p_{t,in}$, total temperature $T_{t,in}$ and flow angle α_{in} at the inlet and the static pressure at the outflow p_{out} to be prescribed, hence $Ma_{in} = f(p_{out})$. Since the application of a controller in this case is non-trivial and will delay the statistical convergence of SRS, it was decided to take the back-pressure from the fully converged RANS solution, that resulted in $Ma_{in} = 0.6$. The error made is assessed by rerunning the cheaper RANS with a controller set to reach the true Main as obtained in the LES (Fig. 4).

The unstructured high-order mesh has been created as a 2D

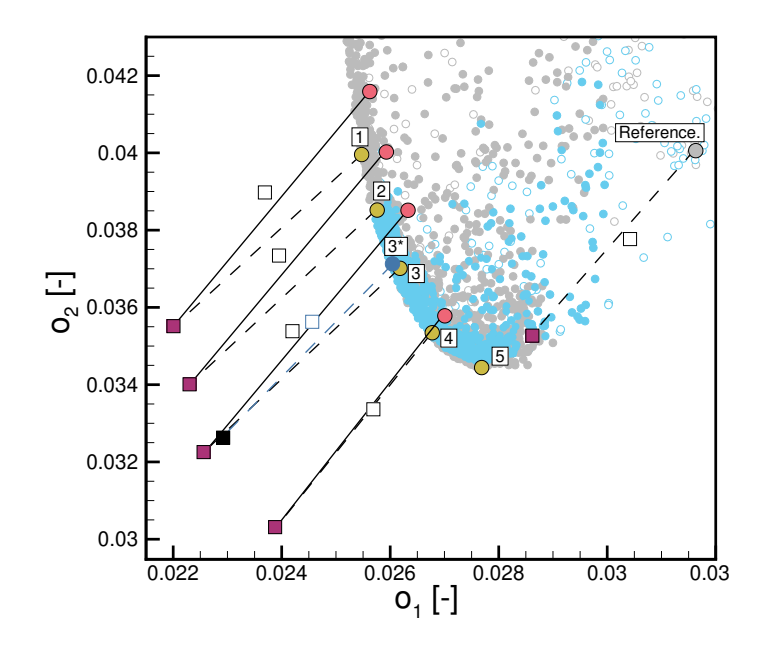


FIGURE 5: Optimization data bases. RANS optimization (•); second RANS optimization with adjusted constraints (•); all constraints met: filled circle (•); not all constraints met: circle (∘); selected geometries of first optimization (•); selected geometry of second optimization (•); LES re-calculation evaluated according to Eq. (3) (■); LES using an alternative loss evaluation (□); RANS resimulation with LES inflow Mach number (•).

mesh with Gmsh [37], which was then uniformly extruded in spanwise direction. In the x-y plane, the mesh consists of 10 616 quadrilaterals. Polynomials of degree 2 have been used to approximate the curved boundary and the 6 layers adjacent to the wall. The 2D mesh is plotted in Fig. 3, showing the benefit of unstructured meshes, being able to locally refine the mesh at relevant locations, i.e. boundary layer and wake region. In spanwise direction, the resolution is kept constant for different spanwise extents, which is 24 elements and, hence, 120 degrees of freedom (DOF) per 0.1c. The mesh resolution at the wall was confirmed to satisfy the y⁺ requirements of wall-resolved LES [12].

Each simulation is started from an initial RANS solution, which has been interpolated onto the fine high-order grid. The LES run for $25t_c$ convective time units, which are defined by the inflow velocity and the chord length as $t_c = c/||\overline{u_1}||$. The line plots have been created with the time-resolved data of volume and boundary probes, which have been sampled with a frequency of $f_s = 10^6 \, \mathrm{Hz} \approx 500/t_c$. The initial transient was automatically detected and removed by the marginal standard error rule (MSER), cf. [38]. For entropy generation analysis, statistical moments of the full 3D flow field have been used, which have been sampled starting at $5t_c$ with the same frequency as probes.

3. OPTIMIZATION STUDY

In order to examine the potential of SRS to support a RANS-based compressor airfoil optimization an optimization study is conducted in this work to incorporate a very limited number of SRS to support a compressor blade optimization based on RANS as outlined in Fig. 4. First, an optimization purely based on

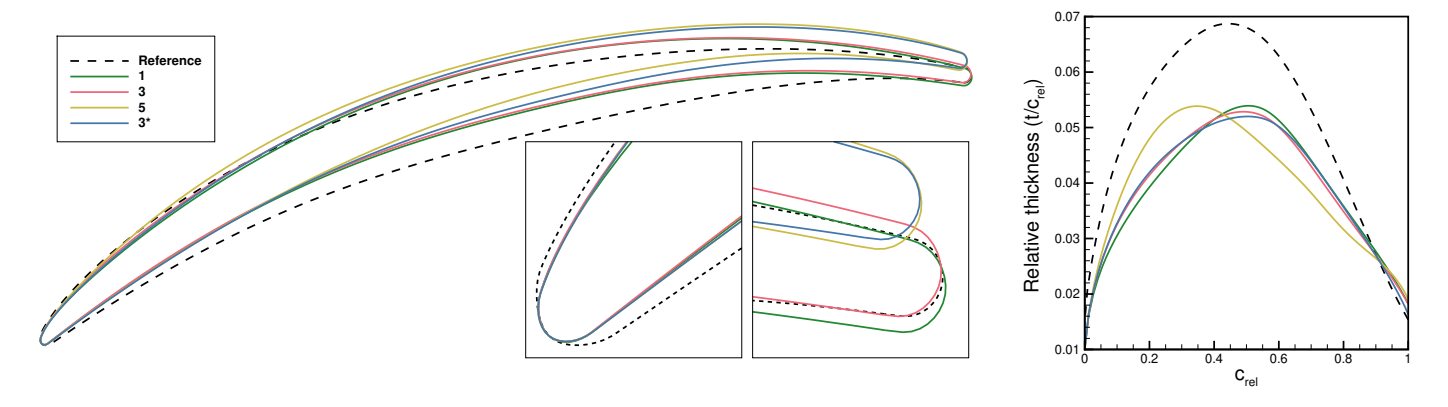


FIGURE 6: Airfoil geometries of reference selected RANS-optimized and selected RANS-optimized with adjusted optimization settings.

RANS is performed, from which a selected number of geometries is re-evaluated using LES, similar to the example given in the introduction Fig. 1, but now on a higher fidelity level. The findings are manually fed back to a second optimization based on RANS, that provides a final geometry, which is re-evaluated using LES to confirm the improvement with respect to the imposed constraints and objectives. The following paragraphs guide through the single steps.

3.1 RANS Optimization

The database of a RANS optimization is shown in Fig. 5 in terms of the two objectives, defined in Eqs. (1) & (2). The highlighted points represent the reference geometry, the Paretofront and a selection of five geometries along the Pareto-front, which will be used to investigate trends along the Pareto-front in the following. The numbering convention used for $\bigcirc 1$ to $\bigcirc 5$ is to have increasing o_1 and hence decreasing o_2 . Compared to the reference geometry a significant loss reduction both at ADP and off-design could be achieved.

3.2 Pareto-front Geometries

The optimized airfoils \bigcirc 1, \bigcirc 3 and \bigcirc 5 along with the reference are shown in Fig. 6 (\bigcirc 3*) is explained in Sec. 3.4). A varying trailing edge angle along the Pareto-front can be observed, affecting also the rear part of the suction and pressure sides. Along the Pareto front, certain parameters vary, while others have largely converged to constant values (Fig. 7). The trailing edge angle decreases, whereas the stagger angle and pitch increase from design \bigcirc 1 to \bigcirc 5. Additionally, suction side spline parameters in the rear part of the blade and near the leading edge, as well as the thickness distribution—thickening in the front and thinning in the rear—show variation. In contrast, the leading edge angle, leading and trailing edge radii, and leading edge asymmetry and shape remain nearly constant along the Pareto front.

Compared to the initial reference geometry the optimized geometries all have increased pitch, LE angle and an increased $(\gamma + \beta_{TE})$. Furthermore, the blade thickness is reduced for the first 90% of the chord (Fig. 7).

Examining the loss polars for the selected geometries (Fig. 8a) the loss improvement can be confirmed. The trade-

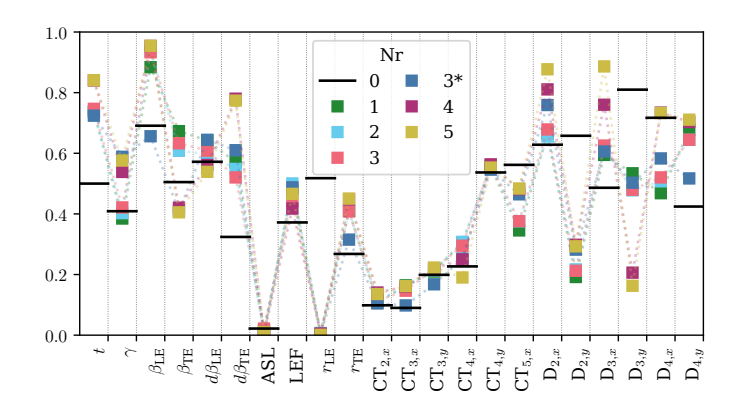


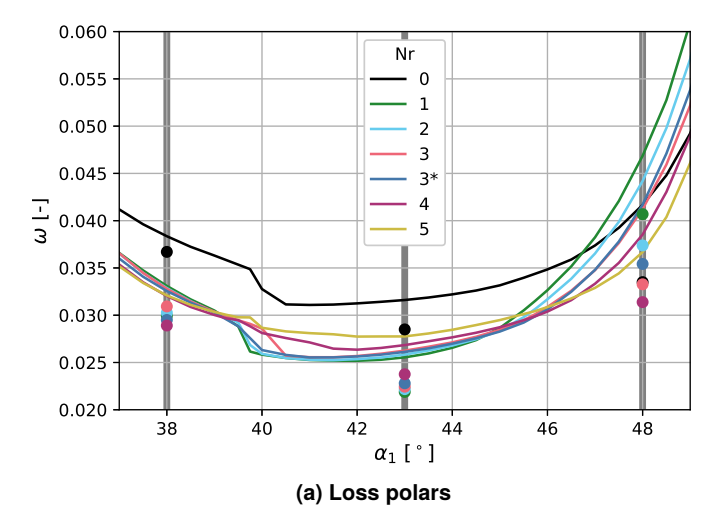
FIGURE 7: Variation of scaled optimization parameters along the selected five Pareto-optimal geometries alongside reference geometry.

off between the two objectives (Eq. (1) and Eq. (2)) along the Pareto-front can mainly be attributed to a trade-off between the loss at OP_{ADP} and OP^+ (steeper polar) or in more global terms between the loss at OP_{ADP} and the working range of the airfoil.

The outflow angle constraints (Tab. 3) are all met, however the optimization converged towards the lower limit at OP^+ for all selected geometries. At OP_{ADP} the outflow angle variation, which lies within the allowed limits, coincides with the loss variation along the Pareto-front.

These observations lead to the following conclusions that can be dawn from the RANS optimization and evaluation of the selected airfoils (1) to (5):

- The increased pitch of all Pareto-front geometries helps reduce overall loss levels.
- Pitch can only be increased as long as constraints on outflow angle are still met. Limiting factor is the outflow angle at increased positive incidence OP⁺.
- Airfoils with lower losses at OP_{ADP} show a reduced working range and higher off-design losses, especially at OP⁺.
- Airfoils with lower losses at design point have an increased outflow angle at design point.



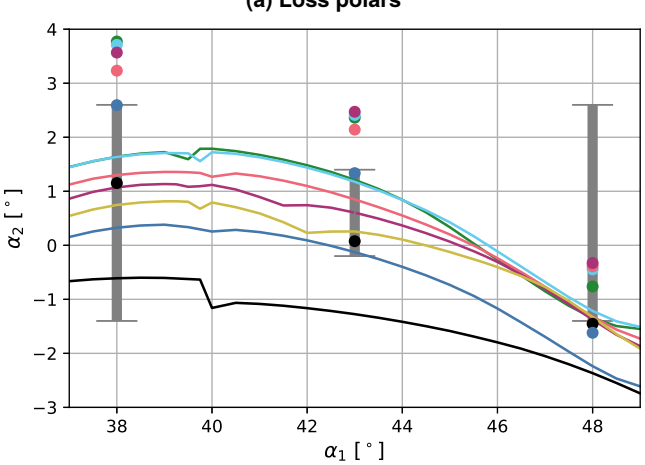


FIGURE 8: Loss polars and outflow angles of reference airfoil and selected optimized airfoils. Solid lines: RANS, dots: LES. The three angles simulated during the optimization are highlighted. Grey bars in (b) indicate the constrained range of α_2 .

(b) Outflow angle vs. inflow angle.

3.3 LES of selected geometries

The selected geometries ① to ④ were evaluated with LES using the same boundary conditions, particularly the backpressure from RANS.

However, the Mach number (Ma_{in}) and consequently Reynolds number (Re_{in}) obtained with LES differ from the RANS values by up to 2% at ADP and OP⁻, and by up to 6% at OP⁺, due to an overprediction of p_{out}/p_{in} with LES. The discrepancies regarding the loss prediction are listed in Tab. 4 and also plotted in Fig. 5 and Fig. 8a in terms of the objectives.

An offset between LES and RANS regarding several flow quantities can be observed, with a clear tendency but slight variations throughout the design space. Fig. 9 plots ω and α_2 for RANS and LES for different OPs. It is visible that for OP⁺ the offset increases for ω , indicating that for increasing incidence the RANS prediction becomes more uncertain. Remarkably the trend is opposite for the outflow angle α_2 . Here the offset increases for OP⁻. Comparing RANS and LES it has to be considered that due to the different losses the LES simulations result in slightly different inflow Ma-numbers compared to the RANS simulations

for the same exit pressure. In order to evaluate the influence of this shift in inflow Mach number, the LES are again re-simulated using RANS matching the inflow Ma-number of the LES, as outlined in Fig. 4. The resulting objectives are plotted in Fig. 5 with lines marking the points that belong to the same geometry. Fig. 9 also shows the results of the re-evaluation with RANS and the matched inflow conditions from LES. It can be observed that the inflow variation mainly affects the loss prediction at OP⁺. This evaluation highlights the importance of accurate and well-defined boundary conditions when comparing different numerical approaches, but also experiments. This will be addressed in more detail in future investigations.

However, the general conclusions that can be drawn on the difference between RANS and LES in the context of this optimization remain unaffected by the mismatch in inflow Mach-number. The differences between RANS and LES remain almost constant with only a slight shift of the adjusted RANS towards the LES. A closer investigation of the isentropic Mach number (Fig. 10) and skin friction coefficient c_f (Fig. 11) underpins this statement. The values are plotted over a relative coordinate along the staggered blade $x_{\rm rel}$, defined by

$$x_{\text{rel}} = \cos\left(\arctan\left(\frac{y}{x}\right) - \alpha_s\right) \frac{\sqrt{x^2 + y^2}}{c},$$
 (6)

where α_s is the stagger angle. The figures exemplary show the results of geometry \Im and \Im^* , which is presented in Sec. 3.5, but are comparable for the other geometries. The most notable observations are

- The aerodynamic loading is increased for the optimized airfoils compared to the reference airfoil.
- RANS and LES agree best at ADP, in particular when comparing against the RANS with adjusted Main, but with a delayed reattachment of the separation bubble on the suction side in the RANS.
- At -5° the flow on the pressure side is strongly accelerated around the LE, resulting in flow separation near the LE, transition to turbulence and reattachment of the flow. The length of the separation bubble is again overestimated in RANS. On the suction side the start of separation matches between RANS and LES, but here the flow reattaches earlier.
- The largest discrepancy have been observed at +5° (cf. Tab. 4), where the error due to a misprediction of the leading edge separation and reattachment propagates downstream.

One major discrepancy between RANS and LES is the difference in the prediction of the outflow angle α_2 (Fig. 8b). The LES shows increased outflow angles at all operating points, up to more than two degrees, i.e. an increased flow turning. Therefore, the constraints of all selected geometries are not met, contradictory to the predictions with RANS. The RANS optimization converged towards geometries that are not meeting the constraints if evaluated with the higher fidelity LES.

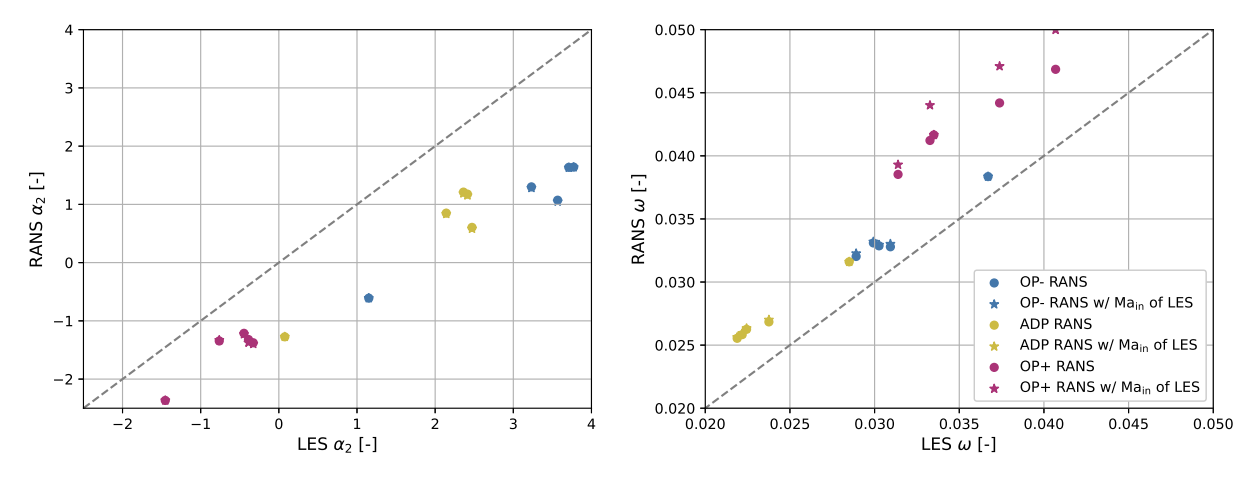


FIGURE 9: Correlation between RANS and LES regarding ω and α_2 at different OPs for airfoils 1-4 and reference.

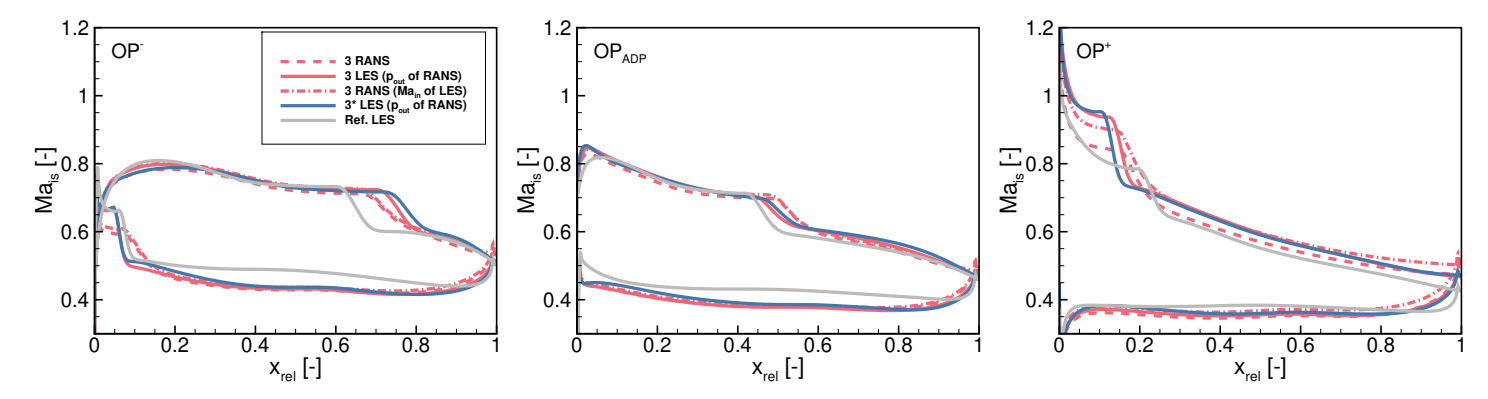


FIGURE 10: Geometry 3, 3* and reference - Ma isentropic. Comparison of RANS result, LES with RANS back pressure, RANS with LES inlet Mach number.

3.4 Adjusted RANS-optimization based on LES data

The LES evaluation of the RANS-optimized airfoil geometries reveals that RANS-based optimization can lead to suboptimal results. To prevent the optimization from converging toward suboptimal designs due to the limitations of the low-fidelity RANS model, it is essential to integrate LES-derived data and insights into the optimization framework.

Balancing the extremely high computational cost of LES with the potential benefits it offers in optimization is a significant challenge. Fully LES-based optimizations are currently impractical for industrial engineering applications, even for relatively simple geometries such as single airfoils, due to the limitations of available computational resources. Therefore it is necessary to develop multi-fidelity optimization frameworks that make use of only a few LES simulations but predominantly rely on RANS. Ideally, LES would only be employed at critical stages of the optimization to validate candidate designs and for operating points that suffer from an increased uncertainty of the RANS prediction due to critical flow features such as separation or transition.

Various approaches with differing levels of complexity can be envisioned to achieve this task. While a detailed exploration of these methods is outside the scope of this paper, our focus is to demonstrate the potential of such strategies by illustrating how RANS-based optimization can lead to sub-optimal geometries and how these shortcomings can be addressed by leveraging LES or other high-fidelity data to identify critical flow prediction inaccuracies and account for them during the optimization process.

Possibilities to make use of LES as a high-fidelity solution in an otherwise RANS-based optimization include:

- Multi-Fidelity meta modelling strategies, such as Co-Kriging.
- LES augmented RANS models, such as data-driven turbulence models.
- Identification of critical flow features and RANS prediction inaccuracies.

While the ultimate goal is to combine the first two approaches to create a highly automated optimization framework for standard industrial design tasks, incorporating LES to achieve unparalleled accuracy, this paper focuses on demonstrating the latter approach in order to evaluate the potential. LES is used to identify critical flow features and to adjust the optimization to account for these effects.

From the LES of \bigcirc to \bigcirc and the reference geometry a shift in outflow angle α_2 can be observed (Fig. 8b) as already stated. This shift has resulted in a convergence of the RANS optimization towards geometries that are not meeting the constraints on outflow angle.

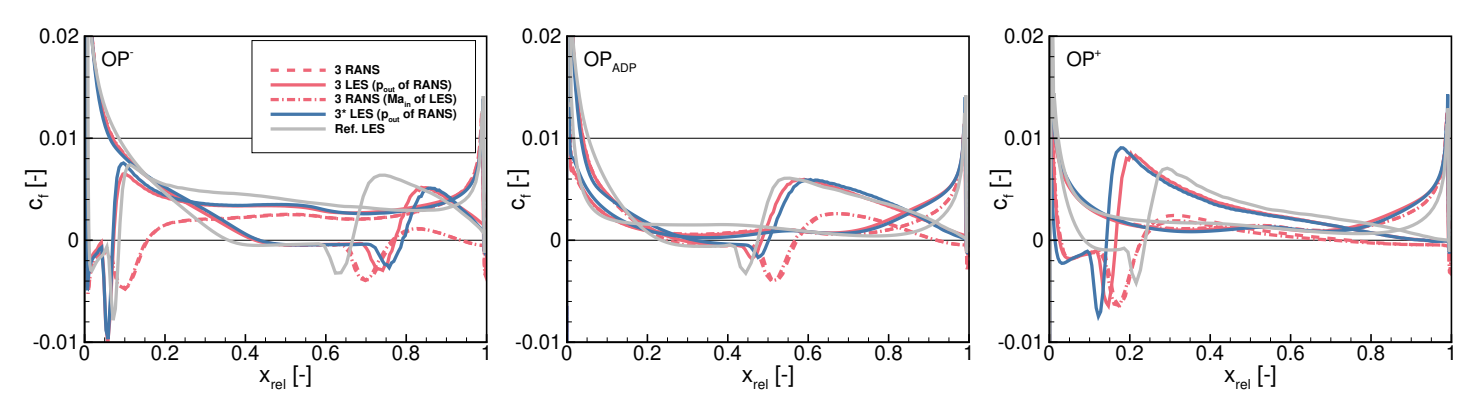


FIGURE 11: Geometry 3, 3* and reference - skin friction coefficient. Comparison of RANS result, LES with RANS back pressure, RANS with LES inlet Mach number.

TABLE 4: Loss comparison according to Eq. (3) between LES and RANS expressed as relative delta. Δ_1 between LES and RANS with $Ma_{in} = 0.6$, Δ_2 between LES and RANS with Ma_{in} adjusted to LES inflow conditions.

		ω_{OP-}			$\omega_{\text{ADP}} = o_1$	Į.		ω_{OP+}			02	
	LES	Δ_1 [%]	Δ_2 [%]	LES	Δ_1 [%]	Δ_2 [%]	LES	Δ_1 [%]	Δ_2 [%]	LES	Δ_1 [%]	Δ_2 [%]
1	0.0300	10.3	10.6	0.0219	16.5	17.1	0.0407	15.3	22.8	0.0353	13.2	17.7
2	0.0303	8.6	8.7	0.0221	16.3	16.9	0.0374	18.2	26.0	0.0338	13.9	18.3
3	0.0309	6.1	6.9	0.0224	17.2	17.3	0.0333	23.8	32.3	0.0321	15.3	20.0
4	0.0289	10.7	11.6	0.0238	12.8	13.7	0.0314	22.7	25.2	0.0301	16.9	18.7

TABLE 5: Adjusted constraints for RANS optimization, taking into account an expected offset between RANS and LES.

Quantity	min	max.
$\alpha_{2.\text{ADP}}$	-1.58	0.02
$\alpha_{2.\mathrm{OP+}}$	-2.24	1.76
$\alpha_{2.\mathrm{OP-}}$	-3.56	0.44

In the context of the airfoil optimization in this study, an unintended increase in the outflow angle of a turbine outlet guide vane would induce swirl in the outflow, leading to reduced thrust and increased losses of the engine. With the knowledge of the discrepancy in predicting the outflow angle with RANS, it is possible to account for the shift in outflow angle α_2 in a second optimization with adjustments made for the constraints. The adjustments made herein for the different operating points are calculated as the mean deviation between RANS and LES results of α_2 for 1 to 4, resulting in the adjusted constraints shown in Tab. 5.

Fig. 5 shows the result of the second RANS optimization compared to the first one. Interestingly most parts of the Pareto-front reach the same values for o_1 and o_2 . However, the outflow angles of the airfoils differ such that the geometries of the second optimization reach lower values of α_2 (Fig. 12). A geometry, termed 3^* , with similar objective values as 3 is selected for further evaluation, see Fig. 6.

3.5 Final optimized airfoil

Re-simulating (3*) with LES confirms, that this airfoil geometry, contrary to (3), satisfies the main constraints (Tab. 3), while maintaining the significant improvements in loss compared

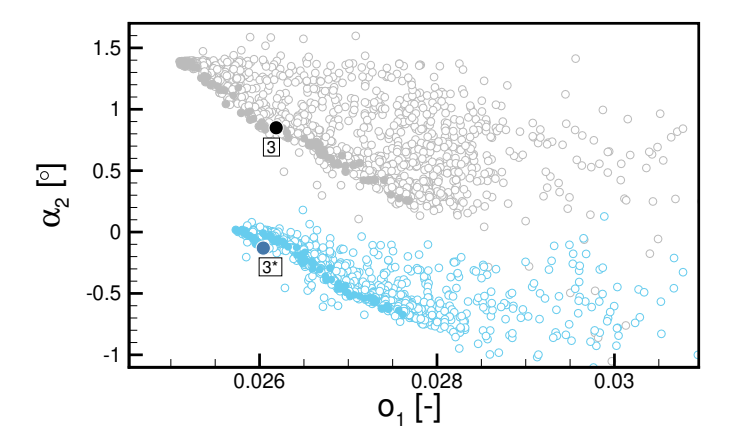


FIGURE 12: Pareto-optimal geometries and optimization data bases. α_2 at OP_{ADP}. RANS optimization: grey; second RANS optimization with adjusted constraints: cyan; circles: data base entries; dots: Pareto-front geometries.

to the reference airfoil. This is also supported by Figs. 10 and 11, which show that the main potential and viscous flow effects are preserved in comparison to \bigcirc 3. Only at OP⁺ the outflow angle constraint is still missed by a slight margin of $\approx 0.2^{\circ}$.

Fig. 6 compares the geometry of 3^* with those of the previous optimization. It can be observed that the thickness distribution and front part of 3^* is almost identical to 3 and mainly the aft part of the airfoil changes with a turning more towards the TE and slightly ($\approx 1^\circ$) reduced.

Overall, the knowledge obtained from the few LES of the first RANS optimization could be used to adjust the RANS-optimization settings in a way that improved the optimization

outcome, especially with regards to the outflow constraints. As a result an airfoil has been found that improves the losses at design point and off-design conditions with a satisfactory fullfilment of the constraints.

4. CONCLUSION & OUTLOOK

A RANS-based optimization of a compressor airfoil was performed with the objective of reducing losses at the design point and off-design conditions, while maintaining an axial outflow. The results demonstrate how constraints drive the optimization towards specific regions of the design space. Simulating the optimized profiles with LES reveals two key findings:

- 1. RANS tends to overpredict losses, with variations depending on the inflow angle and location within the design space;
- 2. The constraints on axial outflow are not met, contradictory to the predictions with RANS.

These findings highlight the limitations of relying solely on RANS-based optimizations, which can lead to suboptimal or even invalid designs. However, incorporating data and insights from SRS, such as LES, to refine the optimization settings of RANS-based frameworks can significantly enhance the results. For the relatively simple case of a cascade optimization, adjusting the constraints on the outflow angle based on LES evaluations of selected profiles proved to be effective in improving the optimization outcome.

This supports the general assumption that RANS-based optimizations can be substantially improved by leveraging data from a limited number of SRS. In the case presented only four Paretooptimal geometries have been simulated using LES. Nonetheless, the presented test case is a simplified 2D scenario, where straightforward correlations between RANS and SRS data were identified. For cases of increasing complexity, such as 3D compressor stages, it becomes more unlikely that similarly simple, almost linear correlations can be derived. Typical 3D industrial optimization tasks must satisfy numerous constraints, including aerodynamic, structural, and geometric requirements. If these constraints are not met, the optimization outcome is often unusable for its intended application and requires modifications. Such adjustments, if feasible at all, degrade the optimization objectives, leading to suboptimal designs. For industry-relevant 3D cases with numerous constraints and complex objectives, automated procedures must be employed. Multi-fidelity strategies such as Co-Kriging are usually the first choice when it comes to combining data of different fidelities, but have their limitations for very sparse high-fidelity data. For 3D geometries with a significantly higher number of free parameters, this challenge becomes even more pronounced. To address this, future research will focus on advanced methodologies that leverage complex data of few SRS, such as data-driven turbulence modeling combined with multi-fidelity surrogate modeling suited to handling sparse high-fidelity data and various locally augmented RANS models. The combination of these approaches offers a promising path forward for efficiently integrating SRS data into RANS-based optimization frameworks for industrial applications.

ACKNOWLEDGMENTS

The authors would like to thank the European Union for funding their research under grant number 101138080 (Project Sci-Fi-Turbo). Views and opinions expressed are however those of the author(s) only and do not necessarily reflect those of the European Union. Neither the European Union nor the granting authority can be held responsible for them.

Moreover, the authors gratefully acknowledge the scientific support and HPC resources provided by the German Aerospace Center (DLR). All simulations in this work have been carried out on the HPC system CARA which is partially funded by the 'Saxon State Ministry for Economic Affairs, Labour and Transport' and the German 'Federal Ministry for Economic Affairs and Climate Action'.

REFERENCES

- [1] Drela, M. and Giles, M. B. "Viscous-inviscid analysis of transonic and low Reynolds number airfoils." *AIAA journal* Vol. 25 No. 10 (1987): pp. 1347–1355. DOI 10.2514/3.9789.
- [2] Youngren, H. and Drela, M. "Viscous/inviscid method for preliminary design of transonic cascades." 27th Joint Propulsion Conference: p. 2364. 1991. DOI 10.2514/6.1991-236.
- [3] Goinis, G., Stollenwerk, S., Nicke, E. and Kügeler, E. "Steady State Versus Time-Accurate CFD in an Automated Airfoil Section Optimization of a Counter Rotating Fan Stage." Vol. Volume 7: Turbomachinery, Parts A, B, and C: pp. 1363–1373. 2011. DOI 10.1115/GT2011-46190.
- [4] Schnoes, M., Schmitz, A., Goinis, G. and Voss, C. "Strategies for Multi-Fidelity Optimization of Multi-Stage Compressors with Throughflow and 3D CFD." ISABE 2019. 2019. URL https://elib.dlr.de/129457/.
- [5] Keane, A. J. "Cokriging for Robust Design Optimization." AIAA Journal Vol. 50 No. 11 (2012): pp. 2351–2364. DOI 10.2514/1.J051391.
- [6] Laurenceau, J. and Sagaut, P. "Building Efficient Response Surfaces of Aerodynamic Functions with Kriging and Cokriging." *AIAA Journal* Vol. 46 No. 2 (2008): pp. 498–507. DOI 10.2514/1.32308.
- [7] Sonoda, T., Yamaguchi, Y., Arima, T., Olhofer, M., Sendhoff, B. and Schreiber, H.-A. "Advanced High Turning Compressor Airfoils for Low Reynolds Number Condition—Part I: Design and Optimization." *Journal of Turbomachinery* Vol. 126 No. 3 (2004): pp. 350–359. DOI 10.1115/1.1737780.
- [8] Schreiber, H.-A., Steinert, W., Sonoda, T. and Arima, T. "Advanced High-Turning Compressor Airfoils for Low Reynolds Number Condition—Part II: Experimental and Numerical Analysis." *Journal of Turbomachinery* Vol. 126 No. 4 (2004): pp. 482–492. DOI 10.1115/1.1737781.
- [9] Hergt, A., Hage, W., Grund, S., Steinert, W., Terhorst, M., Schongen, F. and Wilke, Y. "Riblet Application in Compressors: Toward Efficient Blade Design." *Journal of Turbomachinery* Vol. 137 No. 11 (2015): p. 111006. DOI 10.1115/1.4031090.

- [10] Steinert, W., Fuchs, R. and Starken, H. "Inlet Flow Angle Determination of Transonic Compressor Cascades." *Journal of Turbomachinery* Vol. 114 No. 3 (1992): pp. 487–493. DOI 10.1115/1.2929169.
- [11] Hergt, A., Klinner, J., Grund, S., Willert, C., Steinert, W. and Beversdorff, M. "On the Importance of Transition Control at Transonic Compressor Blades." *Journal of Turbomachinery* Vol. 143 No. 3 (2021): p. 031007. DOI 10.1115/1.4049783.
- [12] Bergmann, M., Morsbach, C., Möller, F. M., Klose, B. F., Hergt, A. and Goinis, G. "A comparitive study of varying incidence angle effects on a low-Reynolds-number compressor cascade based on experiments, low-fidelity and high-fidelity numerical simulations." *Proceedings of the 16th European Turbomachinery Conference (ETC16) Turbomachinery, Fluid Dynamics and Thermodynamics, March 24-28, 2025; Hannover, Germany.*
- [13] Hemmert-Pottmann, S., Forsthofer, N., Voß, C. and Schneider, T. "High-dimensional multi-fidelity optimisation of a 2.5 stage low pressure compressor." *ISABE*. 2019. URL https://elib.dlr.de/129783/.
- [14] Goinis, G., Voß, C. and Nicke, E. "The Potential of Casing Treatments for Transonic Compressors: Evaluation Based on Axial-Slot and Rotor Blade Optimization." 2019. IS-ABE. URL https://elib.dlr.de/130658/.
- [15] Automated Optimization of an Axial-Slot Type Casing Treatment for a Transonic Compressor, Vol. Volume 6B: Turbomachinery of Turbo Expo: Power for Land, Sea, and Air (2013). DOI 10.1115/GT2013-94765.
- [16] Voß, C., Backhaus, J., Siggel, M. and Pahs, A. "A differentiated geometry bladeparameterization methodology for gasturbines." *PREPRINT available at Research Square* (2023)DOI 10.21203/rs.3.rs-3724429/v1.
- [17] Morsbach, C. and di Mare, F. "Conservative segregated solution method for turbulence model equations in compressible flows." 6th European Congress on Computational Methods in Applied Sciences and Engineering (ECCOMAS 2012). 2012.
- [18] Menter, F., Kuntz, M. and Langtry, R. "Ten years of Industrial experience with the SST model." Hanjalić, K., Nagano, Y. and Tummers, M. (eds.). *Turbulence, Heat and Mass Transfer 4*: pp. 625–632. 2003.
- [19] Kato, M. and Launder, B. E. "The Modeling of Turbulent Flow Around Stationary and Vibrating Square Cylinders." *9th Symposium on Turbulent Shear Flows*: pp. 10.4.1–10.4.6. 1993.
- [20] Langtry, R. B. and Menter, F. R. "Correlation-Based Transition Modeling for Unstructured Parallelized Computational Fluid Dynamics Codes." *AIAA Journal* Vol. 47 No. 12 (2009): pp. 2894–2906. DOI 10.2514/1.42362.
- [21] Schlüß, D., Frey, C. and Ashcroft, G. "Consistent Nonreflecting Boundary Conditions For Both Steady And Unsteady Flow Simulations In Turbomachinery Applications." ECCOMAS Congress 2016 VII European Congress on Computational Methods in Applied Sciences and Engineering, Crete Island, Greece. 2016.

- [22] Giles, M. "UNSFLO: A Numerical Method for the Calculation of Unsteady Flow in Turobmachinery." Technical Report No. GTL 205. Gas Turbine Laboratory, Massachusetts Institute of Technology. 1991. URL http://hdl.handle.net/1721.1/104744.
- [23] Bolinches-Gisbert, M., Robles, D. C., Corral, R. and Gisbert, F. "Prediction of Reynolds Number Effects on Low-Pressure Turbines Using a High-Order ILES Method." *Journal of Turbomachinery* Vol. 142 No. 3 (2020): p. 031002. DOI 10.1115/1.4045776.
- [24] Weber, A. and Sauer, M. "PyMesh Template Documentation." Technical report DLR-IB-AT-KP-2016-34. German Aerospace Center (DLR), Institute of Propulsion Technology, Linder Hoehe, Cologne, Germany. 2016.
- [25] Bergmann, M., Gölden, R. and Morsbach, C. "Numerical investigation of split form nodal discontinuous Galerkin schemes for the implicit LES of a turbulent channel flow." *7th European Conference on Computational Fluid Dynamics* (2018).
- [26] Bergmann, Michael. "A split-form discontinuous Galerkin spectral element framework for scale-resolving simulations of turbomachinery flows." doctoral thesis, Ruhr-Universität Bochum, Universitätsbibliothek. 2024. DOI 10.13154/294-10845.
- [27] Bergmann, M., Morsbach, C., Klose, B. F., Ashcroft, G. and Kügeler, E. "A Numerical Test Rig for Turbomachinery Flows Based on Large Eddy Simulations With a High-Order Discontinuous Galerkin Scheme—Part I: Sliding Interfaces and Unsteady Row Interactions." *Journal of Turbomachinery* Vol. 146 No. 2 (2023): p. 021005. DOI 10.1115/1.4063734.
- [28] Klose, B. F., Morsbach, C., Bergmann, M., Hergt, A., Klinner, J., Grund, S. and Kügeler, E. "A Numerical Test Rig for Turbomachinery Flows Based on Large Eddy Simulations With a High-Order Discontinuous Galerkin Scheme—Part II: Shock Capturing and Transonic Flows." *Journal of Turbomachinery* Vol. 146 No. 2 (2023): p. 021006. DOI 10.1115/1.4063827.
- [29] Morsbach, C., Bergmann, M., Tosun, A., Klose, B. F., Bechlars, P. and Kügeler, E. "A Numerical Test Rig for Turbomachinery Flows Based on Large Eddy Simulations With a High-Order Discontinuous Galerkin Scheme—Part III: Secondary Flow Effects." *Journal of Turbomachinery* Vol. 146 No. 2 (2023): p. 021007. DOI 10.1115/1.4063511.
- [30] Bassi, F. and Rebay, S. "A High-Order Accurate Discontinuous Finite Element Method for the Numerical Solution of the Compressible Navier–Stokes Equations." *Journal of Computational Physics* Vol. 131 No. 2: pp. 267–279. DOI https://doi.org/10.1006/jcph.1996.5572.
- [31] Gassner, G. J., Winters, A. R. and Kopriva, D. A. "Split form nodal discontinuous Galerkin schemes with summation-by-parts property for the compressible Euler equations." *Journal of Computational Physics* Vol. 327 (2016): pp. 39–66. DOI 10.1016/j.jcp.2016.09.013.
- [32] Kennedy, C. A. and Gruber, A. "Reduced Aliasing Formulations of the Convective Terms Within the Navier-Stokes

- Equations for a Compressible Fluid." *Journal of Computational Physics* Vol. 227 No. 3 (2008): pp. 1676–1700. DOI 10.1016/j.jcp.2007.09.020.
- [33] Chi-Wang, S. and Stanley, O. "Efficient implementation of essentially non-oscillatory shock-capturing schemes." *Journal of Computational Physics* Vol. 77 No. 2 (1988): pp. 439–471. DOI 10.1016/0021-9991(88)90177-5.
- [34] Shur, M. L., Spalart, P. R., Strelets, M. K. and Travin, A. K. "Synthetic Turbulence Generators for RANS-LES Interfaces in Zonal Simulations of Aerodynamic and Aeroacoustic Problems." *Flow Turbul. Combus.* Vol. 93 No. 1 (2014): pp. 63–92. DOI 10.1007/s10494-014-9534-8.
- [35] Morsbach, C. and Franke, M. "Analysis of a Synthetic Turbulence Generation Method for Periodic Configurations." Salvetti, Maria Vittoria, Armenio, Vincenzo, Fröhlich, Jochen, Geurts, Bernard J. and Kuerten, Hans (eds.). Direct and Large-Eddy Simulation XI: pp. 169–174. 2019.

- Springer International Publishing, Cham.
- [36] Leyh, S. and Morsbach, C. "The Coupling of a Synthetic Turbulence Generator with Turbomachinery Boundary Conditions." García-Villalba, Manuel, Kuerten, Hans and Salvetti, Maria Vittoria (eds.). *Direct and Large Eddy Simulation XII*. 2020. Springer, Cham.
- [37] Geuzaine, C. and Remacle, J.-F. "Gmsh: A 3-D finite element mesh generator with built-in pre- and post-processing facilities." *International Journal for Numerical Methods in Engineering* Vol. 79 No. 11 (2009): pp. 1309–1331. DOI 10.1002/nme.2579.
- [38] Bergmann, M., Morsbach, C., Ashcroft, G. and Kügeler, E. "Statistical Error Estimation Methods for Engineering-Relevant Quantities From Scale-Resolving Simulations." *Journal of Turbomachinery* Vol. 144 No. 3 (2021). DOI 10.1115/1.4052402. 031005.